Molecular Catalysis 432 (2017) 196–209

Contents lists available at ScienceDirect

Molecular Catalysis

journal homepage: www.elsevier.com/locate/mcat

MCAT

Editor's choice paper

A series of bismuth-oxychloride/bismuth-oxyiodide/graphene-oxide nanocomposites: Synthesis, characterization, and photcatalytic activity and mechanism

Yu-Hsun Lee, Yong-Ming Dai, Jing-Ya Fu, Chiing-Chang Chen *

Department of Science Education and Application, National Taichung University of Education, Taichung 403, Taiwan

ARTICLE INFO

Article history:
Received 24 October 2016
Received in revised form 17 January 2017
Accepted 26 January 2017

Keywords:
Bismuth oxychloride
Bismuth oxyiodide
Graphene oxide
Composites
Photocatalytic
Crystal violet

ABSTRACT

This is the first report that a series of bismuth oxychloride/bismuth oxyiodide/graphene oxide (BiO_mCl_n/BiO_xI_y/GO) nanocomposites with different GO contents are synthesized through a simple hydrothermal method and characterized using X-ray diffraction, transmission electron microscopy, scanning electron microscopy energy-dispersive spectroscopy, Fourier transform infrared, X-ray photoelectron spectroscopy, and diffuse reflectance spectroscopy. The BiO_mCl_n/BiO_xI_y/GO composites exhibit excellent photocatalytic activities in the degradation of crystal violet (CV) and phenol under visible light irradiation. The order of rate constants appears BiOCl/Bi_3O_4Cl/BiOI/$Bi_7O_9I_3$/GO > BiOCl/$Bi_{12}O_{17}Cl_2$/BiOI/GO > BiOCl/$Bi_{12}O_{17}Cl_2$/BiOI/GO > BiOCl/Bi_3O_4Cl/BiOI/$Bi_7O_9I_3$/GO > $Bi_{12}O_{17}Cl_2$/Bi_5O_7I/GO > $Bi_{12}O_{17}Cl_2$/Bi_5O_7I/GO > $Bi_4O_5I_2$ > $Bi_7O_9I_3$ > BiOI > Bi_5O_7I > BiOCl > GO for photocatalytic degradation of CV. The photocatalytic activity of BiOCl/Bi_3O_4Cl/BiOI/$Bi_7O_9I_3$/GO composites reaches a maximum rate constant of 0.422 h^{-1}, which is 2.3 times higher than that of BiOCl/Bi_3O_4Cl/BiOI/$Bi_7O_9I_3$, 9 and 2 times higher than that of BiOI and $Bi_4O_5I_2$, and 18 and 12 times higher than that of BiOCl and Bi_3O_4Cl. When being irradiated, it can produce two major active species, superoxide radical ($O_2^{\bullet -}$) and hydroxyl radical ($^{\bullet}OH$), and a minor active species, singlet oxygen ($^1O_2$), for the CV degradation.

1. Introduction

Semiconductor photo-catalysis driven by visible light has sparked great research interest because it provides a valuable method for solving environmental pollution and energy supply problems. An environmentally potent and cheap photo-catalyst is an important component for practical applications of photo-catalysis [1]. The study of visible-light-driven photo-catalysts has attracted considerable attention as an alternative to the elimination of toxic materials from wastewater. The photo-catalytic degradation of CV dyes was researched using several systems to produce active species including TiO_2 [2], ZnO [3], $BaTiO_3$ [4], BiOI [5], Bi_2WO_6 [6], BiO_xCl_y/BiO_mI_n [7], BiOBr/BiOI [8], $PbBiO_2Br$/BiOBr [9], $SrFeO_{3-x}$/g-C_3N_4 [10], Bi_2SiO_5/g-C_3N_4 [11], and BiOI/GO [12].

A simple and effective strategy for improving the photo-catalytic activity of a photo-catalyst is the incorporation of a hetero-structure because hetero-composites (or heterojunction) have great potential for tuning the desired electronic properties of photo-catalysts and efficiently separating photo-induced electron–hole pairs [13,14]. A new group of advantageous photo-catalysts, BiOX (X = F, Cl, Br, I) [15,16], have demonstrated unusual photo-catalytic efficiency because their unique layered structure features an internal static electric field vertical in each layer that may occasion more effective separation of photo-induced charge carriers. BiOX has received increasing interests because of its suitable energy gaps, stability, and relatively superior photo-catalytic activities [17,18]. It was reported that the band gaps of BiOI [19], BiOBr [8], BiOCl [20], BiO_xCl_y/BiO_mI_n [7], and Bi_2O_3 [21] were 1.75, 2.61, 3.37, 1.78-2.95, and 2.30 eV, respectively. It seemed that the gaps of all these semiconductors were in the visible-light range to catalyze the photocatalytic reaction.

BiOCl, a novel layered ternary semiconductor, has been drawn much attention for its remarkable photo-catalytic performance, which is comparable to or even better than that of TiO_2 because of its open crystalline structure. However, the activity of BiOCl nanosheets is still far from satisfaction owing to the rapid recombination of photogenerated excitons and the indigent harvest of sunlight. However, because the valence band for bismuth oxyiodides (BiO_mI_n) contains mostly I_{5p} and O_{2p} orbitals, whereas the conduction band is based on the Bi_{6p} orbital [22], iodine-poor BiO_mI_n could be demonstrated to have band-gap energy lower than it of Bi_2O_3 but higher than it of BiOI [23]; hence, these materials

* Corresponding author.
E-mail address: ccchen@mail.ntcu.edu.tw (C.-C. Chen).

http://dx.doi.org/10.1016/j.mcat.2017.01.002
2468-8231/

might be used as visible-light responsive photocatalysts. In particular, the structure and composition of BiO_mI_n strongly influence their optical, electronic, oxidizing abilities, and other physicochemical properties, offering an opportunity to obtain novel photocatalysts for effective degradation of environmental and toxic pollutants. Following Keller and Kramer [24] who have first reported the practically unlimited solubility of the BiOX/BiOY (X, Y = Cl, Br, I) systems, several articles were published disclosing the successful synthesis and the unique photocatalytic properties of similar oxyhalide materials. However, the synthesis methods, characterization, and evaluated properties of a series of BiOX/BiOY have remained rare until recently.

Graphene (GR) and its derivatives are excellent electron mediators due to their unique two-dimensional structures and superior conductivity, and have attracted numerous attentions recently [25]. Furthermore, it can be easily produced from graphite, which is cheap and naturally sufficient. According to a report, the theoretically specific surface area of GR reaches 2630 m^2/g. Therefore, it can be used as an ideal support material with improved interfacial contact and enhanced adsorption activity. GR has a powerful but flexible structure with high carrier mobility. Thus, a GR-based hybrid photocatalyst will show excellent photocatalytic efficiency, such as, BiOI/GR [26] and BiOBr/GR [27].

Two specific branches of GR research dealt with graphene oxide (GO) and reduced graphene oxide (rGO). This could be considered as a precursor of semiconductor/GO (or rGO) synthesis by either chemical or thermal processes. A previous study showed that the incorporation of GO with a metal oxide could enhance the photocatalytic activity [28]. Apparently, photocatalysis enhancement through GO is because a conjugate structure provides a pathway for the transport of charge carriers. Song et al. [29] synthesized an Ag/Ag_2CO_3/rGO composite that exhibited enhanced photocatalytic performance for the photocatalytic oxidation of organic pollutants. Metal oxide semiconductors finds unparalleled opportunity in wastewater purifi-cation under UV–vis light, largely encouraged by their divergent admirable features like stability, non-toxicity, ease of preparation, suitable band edge positions and facile generation of active oxygen species in the aqueous medium. Currently, many studies reported that the integration of GO and semiconductor or metal oxide photocatalyst, such as $Bi_4O_5I_2$ [12], BiOI [26], MoS_2 [30], ZnO [31], Co_2O_3/TiO_2 [32], TiO_2 [33], $BiVO_4$ [34], $SrTiO_3$ [35], and $BiFeO_3$ [36], could form hybrid materials with superior photocatalytic activity. It is found that the BiO_xI_y/GO (or rGO, GR) composite shows higher photocatalytic activities than BiO_xI_y and GO (or rGO, GR) do for the photocatalytic degradation of dyes [37,38].

Previous studies showed that the incorporation of GO with a metal oxide could enhance photocatalytic activity. According to our literature search, a series of BiO_mCl_n/BiO_xI_y/GO-assisted photocatalytic degradation of CV dyes under visible light irradiation has never been reported. This study synthesizes a series of BiO_mCl_n/BiO_xI_y/GO nanocomposites with different GO contents, synthesizes through a simple hydrothermal method, and compares their photocatalytic activities in degrading CV in aqueous solutions under visible light irradiation. Possible photo-degradation mechanisms are proposed and discussed in this research. The study is useful in synthesizing BiO_mCl_n/BiO_xI_y/GO and degrading dye for the future applications of environmental pollution and control.

2. Experimental Details

2.1. Materials

Graphite (Showa), isopropanol, H_2SO_4 and HCl (Merck), $KMnO_4$ (Shimakyu), $NaNO_3$, $Bi(NO_3)_3{\bullet}5H_2O$, and KI (Katayama), CV dye (TCI), *p*-benzoquinone (Alfa Aesar), sodium azide (Sigma), and ammonium oxalate (Osaka) were purchased and used without further purification. Reagent-grade sodium hydroxide, nitric acid, ammonium acetate, and high pressure liquid chromatography (HPLC)-grade methanol were obtained from Merck.

2.2. Instruments and analytical methods

Crystallinity and phase analysis was performed by powder X-raydiffraction (XRD) using a MAC Science MXP18 equipped with Cu-Ka radiation and operated at 40 kV and 80 mA. Nanostructures were visualized by high-resolution transmis-sion electron microscopopy (HR-TEM). Images, selected area electron diffraction patterns, high resolution transmission electron microscopic (HRTEM) images, and energy-dispersive X-ray spectra (EDS) were obtained using a JEOL-2010 with an accelerating voltage of 200 kV. Al-Kα radiation was generated at 15 kV. Surface morphology and composition were also visualized by a field emission scanning electron microscope electron-dispersive X-ray spectroscopy (FE-SEM-EDS). FE-SEM-EDS measurement was conducted using a JEOL JSM-7401F at an acceleration voltage of 15 kV. High resolution X-ray photoelectron spectroscopic measurement was conducted using an ULVAC-PHI. Binding energies were corrected to the C 1s peak at 284.6 eV and surface atomic compositions calculated via correction for the appropriate instrument response factors. Photoluminescence (PL) measurement was conducted on Hitachi F-7000. Ultraviolet photoelectron spectroscopic measurement was performed using an ULVAC-PHI XPS, PHI Quantera SXM. Brunauer-Emmett-Teller (BET) specific surface areas of samples (S_{BET}) were measured with an automated system (Micrometrics Gemini) by using nitrogen gas as the adsorbate at liquid nitrogen temperature. Textural properties were characterized by nitrogen porosimetry on a surface area analyzer, to calculate pore size distributions and BET surface areas. The HPLC-PDAESI-MS system consisted of a Waters 1525 binary pump, 2998 photodiode array detector, and 717 plus autosampler, a ZQ2000 micromass detector. LC-MS analysis was undertaken to identify products of CV photodegradation. The amount of residual dye at each reaction cycle was determined by HPLC-PDA. Transmission FT-IR and ATR/FT-IR spectra were acquired with a Nicolet 5700 Fourier Transform Infrared spectrometer (Thermo) equipped with a Greasby-Specac advanced overhead (specaflow) ATR system P/N 1401 series.

2.3. Synthesis of BiO_mCl_n/BiO_xI_y/GO

GO was synthesized by stirring 1 g powdered flake graphite and 0.5 g $NaNO_3$ into 23 mL H_2SO_4 at 0 °C ice bath. While maintaining vigorous agitation, 3 g $KMnO_4$ was added to the suspension. The ice bath was then removed, and the temperature of the suspension was brought to 35 °C and maintained at that temperature overnight. Then, 3 g $KMnO_4$ was added to the suspension, which was allowed to stand for 3 h. After 3 h, 46 mL H_2O was slowly stirred into the paste, causing violent effervescence and the temperature increasing to 95 °C. The diluted suspension, now brown in color, was maintained at this temperature for 15 min. The suspension was then further diluted to approximately 140 mL with warm water and treated with 30% (w) H_2O_2 to reduce the residual MnO_4^- and MnO_2 to bleach soluble $Mn(SO_4)_2$. Upon the treatment with peroxide, the suspension turned bright yellow. The suspension was filtered, and a yellow-brown filter cake was obtained. After washing the cake three times with a total of 140 mL warm water, the GO residue was dispersed in 100 mL of 10% HCl. Dry GO was obtained through centrifugation followed by drying in the oven at 60 °C overnight [12,39].

Five mmol $Bi(NO_3)_3{\cdot}5H_2O$ was first mixed in a 50-mL flask and then added 5 mL 4 M ethylene glycerol and GO powder. With con-

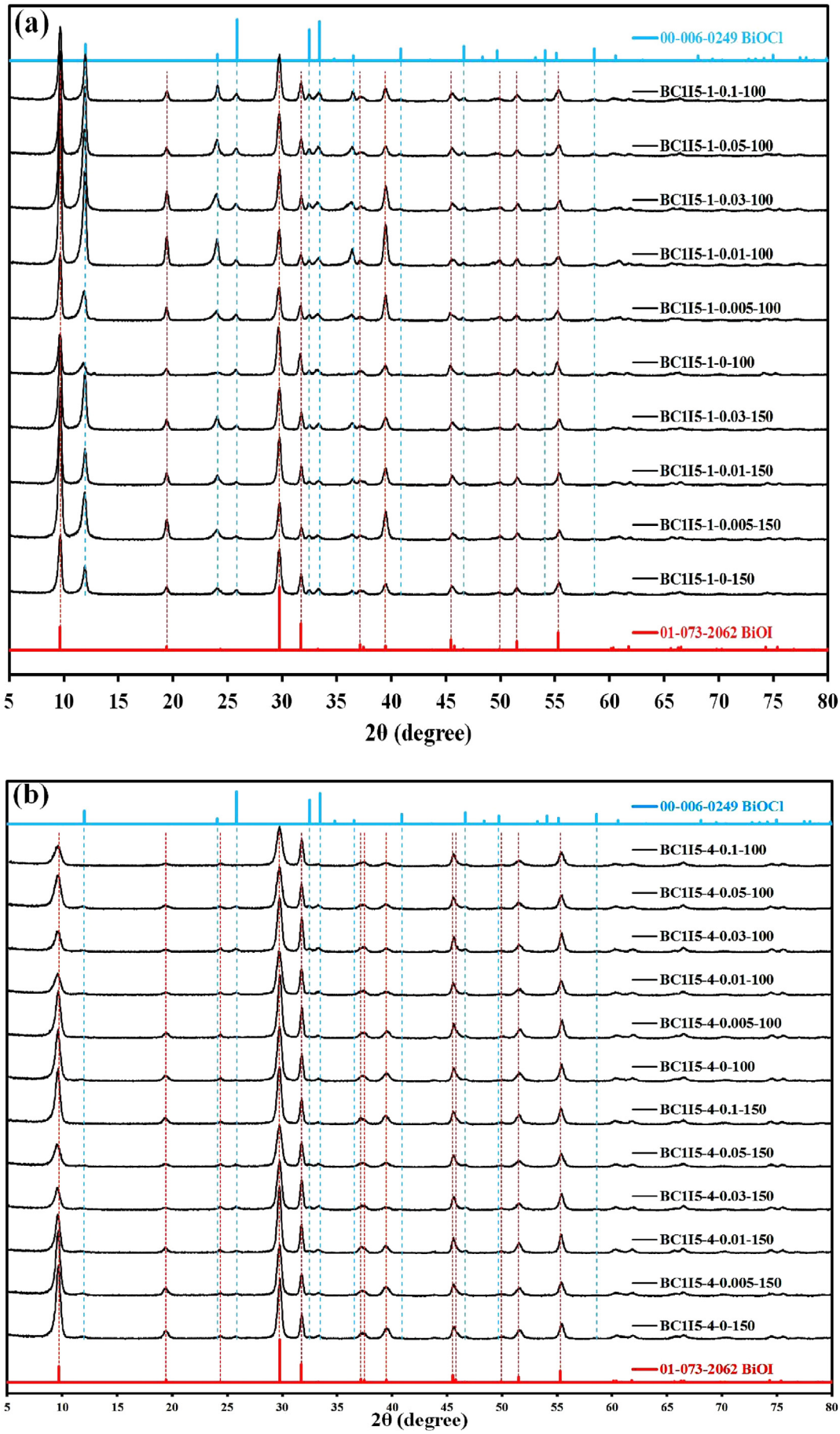

Fig. 1. XRD patterns of as-prepared BiO_pCl_q/BiO_xI_y/GO samples under different conditions. (pH = 1–13, temp = 100–150 °C, $Bi(NO_3)_3{\cdot}5H_2O$ = 2.42 g, GO = 0.05–0.03 g, KI = 15 mmol, KCl = 3 mmol).

tinuous stir, 2 M NaOH was added dropwise to adjust the pH value; when a precipitate was formed, 2 mL KI and KCl were also added dropwise. The solution was then stirred vigorously for 30 min and transferred into a 30 mL Teflon-lined autoclave, which was heated to 100–250 °C for 12 h and then naturally cooled to room temperature. The resulting solid precipitate was collected by filtration, washed with deionized water and methanol to remove any possible ionic species in the solid precipitate, and then dried at 60 °C overnight. Depending on the molar ratio of $Bi(NO_3)_3 \bullet 5H_2O$ to KI or KCl, pH value, temperature, and time, different BiO_mCl_n/BiO_xI_y/GO samples could be synthesized.

2.4. Photocatalytic and active species experiments

CV irradiation experiments were conducted on a stirred aqueous solution contained in a 100-mL flask; the aqueous suspension of CV (100 mL, 10 ppm) and a catalyst powder were placed in a Pyrex flask. The pH of the suspension was adjusted by adding either NaOH or HNO_3 solution. Dark experiments were performed to examine the adsorption or desorption equilibrium. Ten mg photocatalyst was mixed with 100 mL aqueous CV solution with a known initial concentration in a 100-mL flask, and the mixture was shaken in an orbital shaker (100 rpm) at a constant temperature. The mixture was centrifuged at 3000 rpm in a centrifugation machine after batch sorption experiments so that the absorbance of CV could be determined at 580 nm through HPLC photo-diode array electrospray ionization mass spectrometry (HPLC-PDA-ESI-MS). The concentrations of the solutions were determined using a linear regression equation. Prior to irradiation, the suspension was magnetically stirred in the dark for approximately 30 min to establish an adsorption or desorption equilibrium between the CV and the catalyst surface. Irradiation was conducted using 150 W Xe arc lamps with the light intensity fixed at 31.1 W/m^2, and the reaction vessel was placed 30 cm from the light source. At given irradiation time intervals, a 5-mL aliquot was collected and centrifuged to remove the catalyst. The supernatant was measured using HPLC-PDA-ESI-MS.

A series of quenchers were introduced to scavenge the relevant active species to evaluate the effect of the active species during the photocatalytic reaction. Superoxide radical, hydroxyl radical, hole, and singlet oxygen ($^1O_2$) were studied by adding 1.0 mM benzoquinone (BQ, a quencher of superoxide radical) [40], 1.0 mM isopropanol (IPA, a quencher of hydroxyl radical) [41], 1.0 mM ammonium oxalate (AO, a quencher of hole) [42], and 1.0 mM sodium azide (SA, a quencher of singlet oxygen) [43]. The method was similar to the previously reported photocatalytic activity test.

3. Results and Discussion

3.1. Characterization of BiO_mCl_n/BiO_xI_y/GO heterojunction

3.1.1. Phase structure

Fig. 1 shows the XRD patterns of the as-prepared samples; the patterns clearly show the existence of different BiO_mCl_n/BiO_xI_y phase composites with GO. All the as-prepared samples contain BiOCl phase (JCPDS 06-0249), Bi_3O_4Cl phase (JCPDS 36-0760), $Bi_{12}O17Cl_2$ phase (JCPDS 37-0702), BiOI phase (JCPDS 73-2062), $Bi_7O_9I_3$ phase [44], Bi_5O_7I phase (JCPDS 40-0548), and GO [45]. At pH = 1, the XRD patterns (Fig. 1(a)) are identical to those reported for BiOCl/BiOI/GO ternary phases; at pH = 4, the XRD patterns (Fig. 1(b)) are identical to those reported for BiOCl/BiOI/GO ternary phases; at pH = 7, the XRD patterns (Fig. 1(c)) are identical to those reported for BiOCl/Bi_3O_4Cl/BiOI/$Bi_7O_9I_3$/GO pentabasic phases; at pH = 10, the XRD patterns (Fig. 1(d)) are identical to those reported for BiOCl/$Bi_{12}O_{17}Cl_2$/BiOI/$Bi_7O_9I_3$/GO pentabasic phases; and, at pH = 13, the XRD patterns (Fig. 1(d)) are identical to those reported for $Bi_{12}O_{17}Cl_2/Bi_5O_7I$/GO ternary phases. Table 1 summarizes the results of the XRD measurement.

In Fig. 2, the HRTEM image shows that four sets of different lattice images are found with a d-spacing of 0.3440, 0.4004, 0.2692, and 0.3170 nm, corresponding to the (101) plane of BiOCl, the (011) plane of Bi_3O_4Cl, the (111) plane of BiOI, and the (012) plane of $Bi_7O_9I_3$, which is in satisfactory agreement with the XRD results (Fig. 1(c)). The results suggest that the series of BiO_xI_y/GO phases are produced in the composites, which are favorable for the separation of photoinduced carriers, yielding high photocatalytic activities.

The results illustrate that, at different pH values, a series of changes occur in the products. The proposed processes for the formation of BiO_mCl_n/BiO_xI_y/GO composites are described in

Table 1
Crystalline phase changes of BiO_pCl_q/BiO_xI_y/GO prepared under different reaction conditions. (◆ BiOI, ■ $Bi_7O_9I_3$, ● Bi_5O_7I, ◇ BiOCl, □ Bi_3O_4Cl, ○ $Bi_{12}O_{17}Cl_2$, ▼ GO).(For interpretation of the references to colour in this table, the reader is referred to the web version of this article.)

BiO_pCl_q/BiO_xI_y/GO (100 °C)					
Graphene oxide Weight (g)	pH				
	1	4	7	10	13
0	◆◇	◆◇	◆◇■□	◆◇■○	●○
0.005	◆◇▼	◆◇▼	◆◇■□▼	◆◇■○▼	●○▼
0.01	◆◇▼	◆◇▼	◆◇■□▼	◆◇■○▼	●○▼
0.03	◆◇▼	◆◇▼	◆◇■□▼	◆◇■○▼	●○▼
0.05	◆◇▼	◆◇▼	◆◇■□▼	–	–
0.1	◆◇▼	◆◇▼	–	–	–
BiO_pCl_q/BiO_xI_y/GO (150 °C)					
Graphene oxide Weight (g)	pH				
	1	4	7	10	13
0	◆◇	◆◇	◆◇■□	◆◇■○	●○
0.005	◆◇▼	◆◇▼	◆◇■□▼	◆◇■○▼	●○▼
0.01	◆◇▼	◆◇▼	◆◇■□▼	◆◇■○▼	●○▼
0.03	◆◇▼	◆◇▼	◆◇■□▼	◆◇■○▼	●○▼
0.05	–	◆◇▼	◆◇■□▼	–	●○▼
0.1	–	◆◇▼	–	–	–

Eqs. (1)–(15). The results explain that a series of changes in the compounds occur at different hydrothermal conditions, expressed as $BiOCl \rightarrow Bi_4O_5Cl_2 \rightarrow Bi_{24}O_{31}Cl_{10} \rightarrow Bi_3O_4Cl \rightarrow Bi_{12}O_{17}Cl_2 \rightarrow \alpha$-$Bi_2O_3$ and $BiOI \rightarrow Bi_4O_5I_2 \rightarrow Bi_7O_9I_3 \rightarrow Bi_3O_4I \rightarrow Bi_5O_7I \rightarrow \alpha$-$Bi_2O_3$. By controlling the pH of the hydrothermal reaction, different compositions of bismuth oxyhalides are obtained.

$$Bi^{3+} + 3Cl^- \rightarrow BiCl_{3(s)} \quad (1)$$

$$BiCl_{3(s)} + 2OH^- \rightarrow BiOCl_{(s)} + 2Cl^- + H_2O \quad (2)$$

$$4BiOCl_{(s)} + 2OH^- \rightarrow Bi_4O_5Cl_{2(s)} + 2Cl^- + H_2O \quad (3)$$

$$6Bi_4O_5Cl_{2(s)} + 2OH^- \rightarrow Bi_{24}O_{31}Cl_{10(s)} + 2Cl^- + H_2O \quad (4)$$

$$Bi_{24}O_{31}Cl_{10(s)} + 2OH^- \rightarrow 8Bi_3O_4Cl_{(s)} + 2Cl^- + H_2O \quad (5)$$

$$5Bi_3O_4Cl_{(s)} + 2OH^- \rightarrow 3Bi_5O_7Cl_{(s)} + 2Cl^- + H_2O \quad (6)$$

$$12Bi_5O_7Cl_{(s)} + 2OH^- \rightarrow 5Bi_{12}O_{17}Cl_{2(s)} + 2Cl^- + H_2O \quad (7)$$

$$Bi_{12}O_{17}Cl_{2(s)} + 2OH^- \rightarrow 6Bi_2O_{3(s)} + 2Cl^- + H_2O \quad (8)$$

$$Bi^{3+} + 3I^- \rightarrow BiI_{3(s)} \quad (9)$$

$$BiI_{3(s)} + 2OH^- \rightarrow BiOI(s) + 2I^- + H_2O \quad (10)$$

$$4BiOI_{(s)} + 2OH^- \rightarrow Bi_4O_5I_{2(s)} + 2I^- + H_2O \quad (11)$$

$$7Bi_4O_5I_{2(s)} + 2OH^- \rightarrow 4Bi_7O_9I_{3(s)} + 2I^- + H_2O \quad (12)$$

$$3Bi_7O_9I_{3(s)} + 2OH^- \rightarrow 7Bi_3O_4I_{(s)} + 2I^- + H_2O \quad (13)$$

$$5Bi_3O_4I_{(s)} + 2OH^- \rightarrow 3Bi_5O_7I_{(s)} + 2I^- + H_2O \quad (14)$$

$$2Bi_5O_7I_{(s)} + 2OH^- \rightarrow 5Bi_2O_{3(s)} + 2I^- + H_2O \quad (15)$$

Fig. 3 shows the Fourier transform infrared (FT-IR) spectra of the BiOCl/Bi_3O_4Cl/BiOI/$Bi_7O_9I_3$/GO composites produced at different weight percentages, where a strong absorption is located mainly in the range of 400–750 cm^{-1}, as a result of the stretching vibrations of Bi—O—Cl, Bi—O—I, Bi—O, and Bi—O—Bi in bismuth oxychlorides/bismuth oxyiodide composites [5]. The FT-IR spectra of GO show a strong absorption band at 3429 cm^{-1} because of the O—H stretching vibration. The spectra also exhibit bands at approximately 1726 cm^{-1} because of the C=O stretching of COOH groups situating at the edges of GO sheets, and the O—H bending vibration, epoxide groups, and skeletal ring vibrations were observed at approximately 1630 cm^{-1} [46]. The absorption at 1395 and 1001 cm^{-1} may be attributed to tertiary C—OH and the stretching of C—O—C groups. After the composition process, the intensity of the absorption bands because of the O—H stretching vibration (3428 cm^{-1}) and C=O stretching vibration (1725 cm^{-1}) decreases substantially, and the band at 1630 cm^{-1} is absent [47]. Instead, a new absorption band appears at 1569 cm^{-1}, which is attributed to the skeletal vibration of graphene sheets [48]. This result agrees with that of the XRD and TEM experiments.

3.1.2. X-ray photoelectron spectroscopic analysis

XPS is used for measuring the purity of the prepared samples. The spectra presented in Fig. 4 are Bi 4f, O 1s, Cl 2p, and I 3d for the BiOCl/Bi_3O_4Cl/BiOI/$Bi_7O_9I_3$/GO samples. The transition peaks involving in these spectra orbitals demonstrate that the catalysts are composed of Bi, O, Cl, I, and C (Fig. 4(a)). The characteristic binding energy value of 157.5-158.4 eV for Bi $4f_{7/2}$ (Fig. 4(b)) shows a trivalent oxidation state for bismuth. An additional spin–orbit doublet with binding the energy of 155.2-156.0 eV for Bi $4f_{7/2}$ is also revealed o all samples, suggesting that certain parts of bismuth exist in the (+3−x) valence state. This shows that the trivalent bismuth is partially reduced to the lower valence state through the hydrothermal method. A similar chemical shift of approximately 2.0 eV for Bi $4f_{7/2}$ was published by Liao et al. [5,49]. They found that the $Bi^{(+3-x)}$

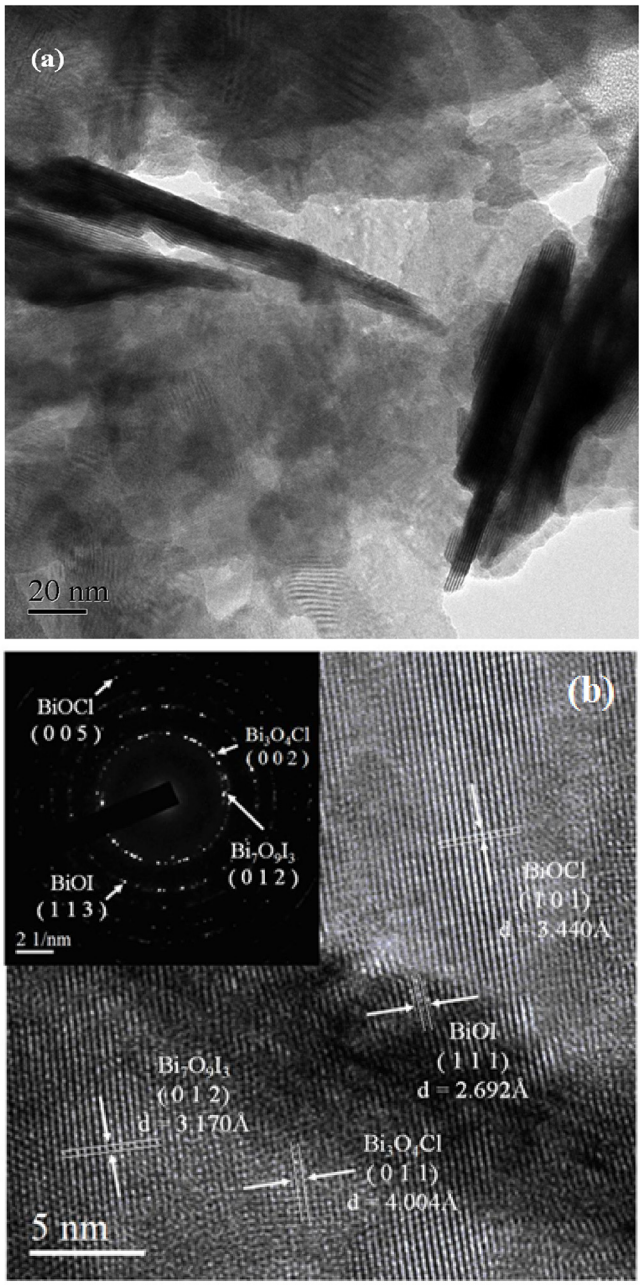

Fig. 2. FE-TEM of as-prepared BiOCl/Bi_3O_4Cl/BiOI/$Bi_7O_9I_3$/GO (pH = 7, 0.03 g GO).

formal oxidation state could most probably be ascribed to the sub-stoichiometric forms of Bi within the Bi_2O_2 layer, and the formation of the low oxidation state results in oxygen vacancies in the crystal lattice. However, this study assumes that the $Bi^{(+3-x)}$ formal oxidation state could most likely be ascribed to the sub-stoichiometric forms of Bi at the outer site of the particles, and the formation of the low oxidation state results in oxygen vacancies in the crystal surface, revealing that the main chemical states of the bismuth element in the samples are not trivalent. Fig. 4(c) shows the high-resolution XPS spectra for the O 1s region of BiO_mCl_n/BiO_xI_y/GO composites, which could be resolved into two peaks; the main peak at 528.7 eV is attributed to the Bi—O bonds in the $(Bi_2O_2)^{2+}$ slabs of the BiOX layered structure, whereas the peak at 531.0 eV is assigned to the hydroxyl groups on the surface [50]. From Fig. 4(d), the binding energy of 198.4 eV and 196.7 eV is attributed to Cl $2p_{3/2}$ and $2p_{1/2}$, respectively, which could be pointed to Cl at the monova-

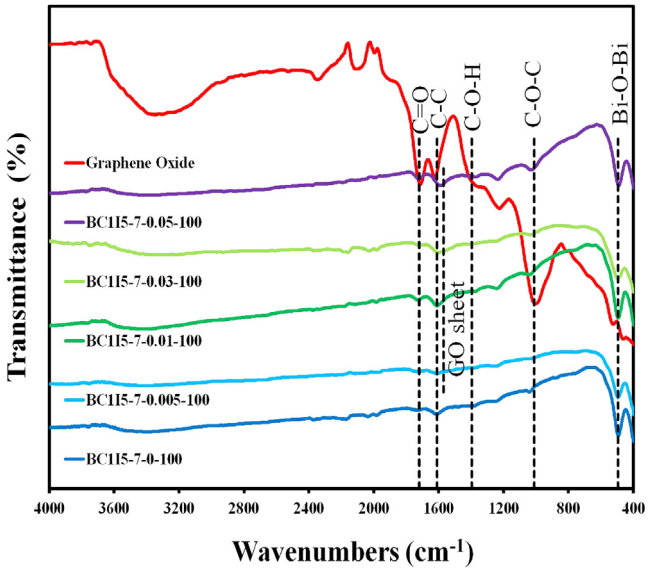

Fig. 3. FT-IR of as-prepared BiOCl/Bi_3O_4Cl/$Bi_7O_9I_3$/BiOI/GO samples under different GO weight at pH = 7.

lent oxidation state. From Fig. 4(e), the binding energy of 629.0 eV and 617.5 eV is attributed to I $3d_{5/2}$ and $3d_{3/2}$, respectively, which could be pointed to I at the monovalent oxidation state. Fig. 4(f) and (g) shows the high-resolution C 1 s spectrum of BiO_pCl_q/BiO_xI_y/GO composites and pure GO. Three carbon species are displayed mainly in the C 1 s spectra of pure GO and BiO_pCl_q/BiO_xI_y/GO composites including un-oxidized carbons (sp^2 carbon), C—O, and C═O. As seen in Fig. 4(f) and (g), three different chemically shifted components are consisted, which could be de-convoluted into sp^2 carbons in aromatic rings (284.4 eV) and C atoms bonded to oxygen (C—O 286.8 eV) and carbonyl (C═O, 288.7 eV) [51]. The asymmetric O 1s peak shown in Fig. 4(c) can be split by using the XPS peak-fitting program for pure GO. The peak at 530.0 eV is assigned to the external —OH group or the water molecule adsorbed on the surface, and the other O 1s peak appearing at 528.7 eV corresponds to the C—O bonds in the GO [49].

3.1.3. Morphological structure and composition

A series of BiO_pCl_q/BiO_xI_y/GO composites are synthesized through hydrothermal methods at different pH values. The surface morphologies of the as-prepared samples are measured using FE-SEM-EDS. The FE-SEM image (Fig. 5) displays that the morphologies of the samples acquired at different pH values turn from flower-like to nanosheets and small-thin nanosheets, and then become irregular small-thin nanosheets. The SEM-EDS and TEM-EDS results demonstrate that the main elements within these samples are bismuth, oxygen, chlorine, iodine, and carbon (Table 2). From the aforementioned results, a series of BiO_pCl_q/BiO_xI_y/GO composites could be selectively synthesized through the controlled hydrothermal method.

3.1.4. Optical absorption properties

As shown in Fig. 6 for the diffuse reflectance ultraviolet of various BiO_pCl_q/BiO_xI_y/GO composites, the absorption edge of BiO_pCl_q/BiO_xI_y is about 566.2–733.8 nm, which is originated from its band gap of 1.78–1080 eV and is consistent with the reported results [5]. The E_g value of BiO_pCl_q/BiO_xI_y/GO is determined from a plot of $(\alpha h\nu)^{1/2}$ vs. energy ($h\nu$), which is calculated as 1069–2.63 eV (Table 2). The results suggest that the fabrication of the BiO_pCl_q/BiO_xI_y/GO composites could greatly improve the optical absorption property and increase the utilized efficiency of solar

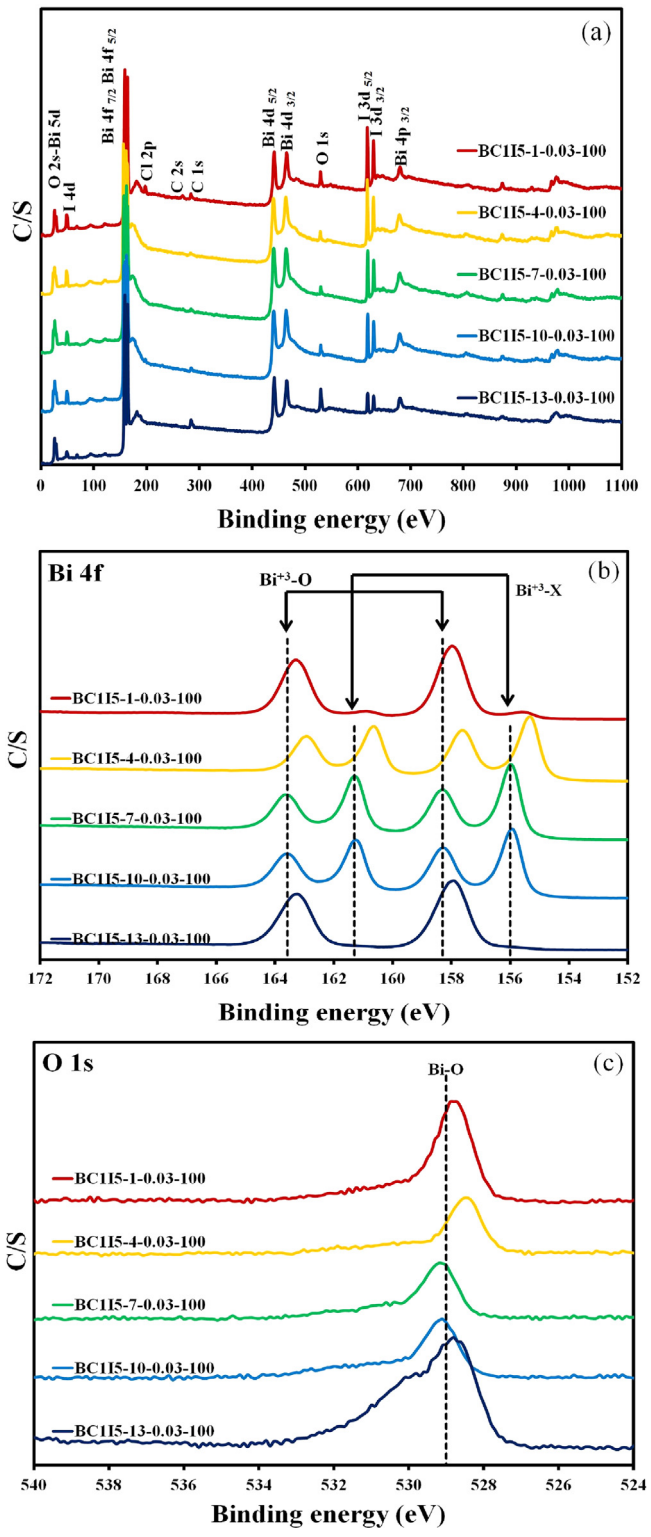

Fig. 4. XPS of BiO_pCl_q/BiO_xI_y/GO survey XPS spectrum at different pH values. (a) total survey, (b) Bi–4f, (c) O–1s, (d) Cl–2p, (e) I–3d, (f) C–1s, (g) 0.03 g GO C–1s (pH = 7).

light, which is favorable for the enhancement of the photocatalytic activity.

3.1.5. Adsorption–desorption isotherm

The BET surface area of GO is measured to be 12.98 m^2g^{-1}; far below the theoretical value of fully exfoliated pristine graphene

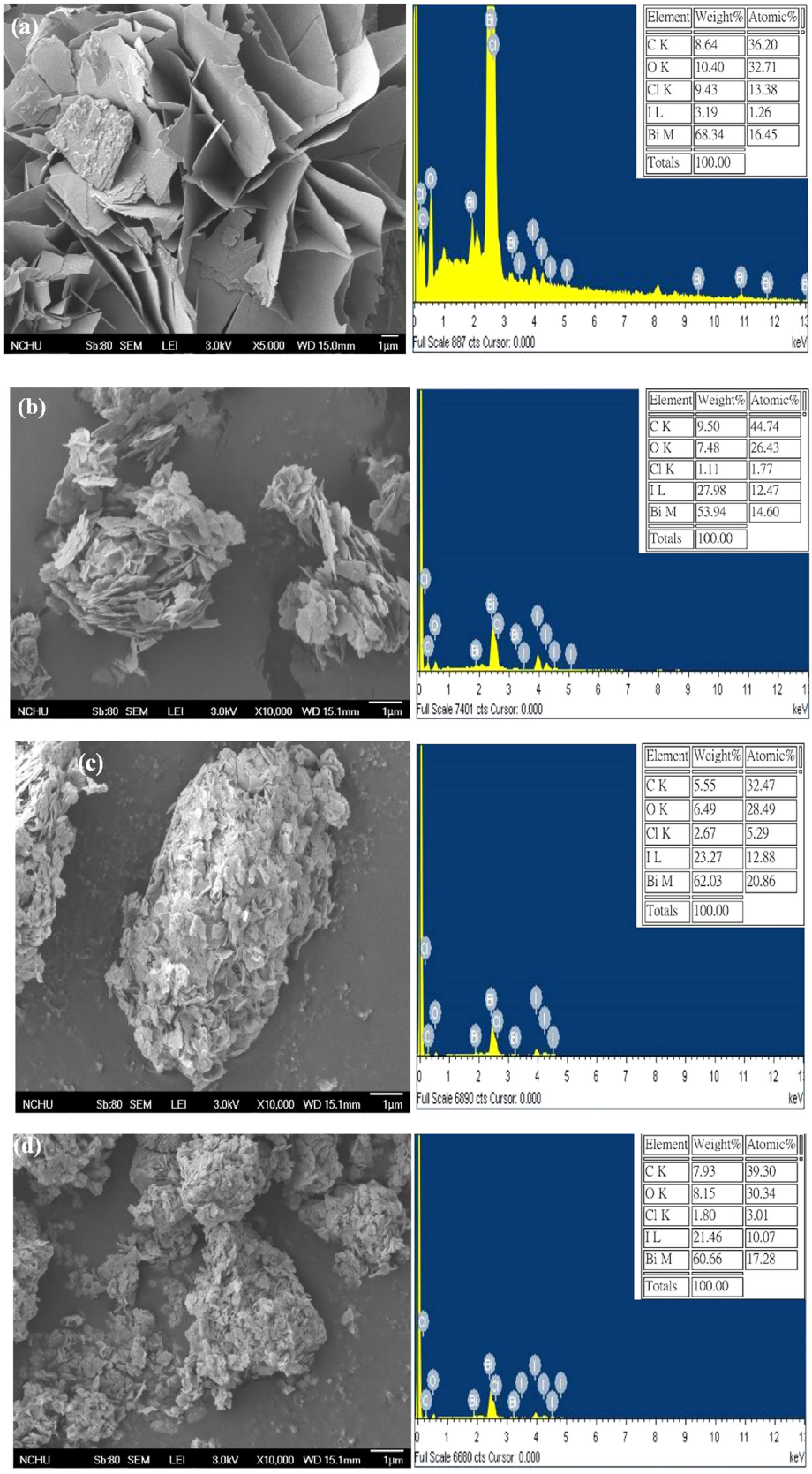

Fig. 5. SEM-EDS of as-prepared samples under different pH values. (Temp = 100 °C, $Bi(NO_3)_3 \cdot 5H_2O$ = 2.42 g, GO = 0.03 g, KI = 15 mmol, KCl = 3 mmol). (a) BiOCl/BiOI/GO, (b) BiOCl/BiOI/GO, (c) BiOCl/Bi_3O_4Cl/BiOI/$Bi_7O_9I_3$/GO, and (d) BiOCl/$Bi_{12}O_{17}Cl_2$/BiOI/GO.

Table 2
Physical and chemical properties of BiO_pCl_q/BiO_xI_y/GO samples prepared under different reaction conditions.

Photocatalysts	EDS of atomic ratio (%)					BET Surface Area (m^2g^{-1})	E_g
	Bi	O	Cl	I	C		
BC1I5-1-0.01-150	25.79	40.42	18.13	2.81	12.86	–	1.78
BC1I5-4-0.01-150	29.3	30.19	5.59	23.37	11.56	–	1.87
BC1I5-7-0.01-150	25.5	38.16	5.49	17.84	13.01	–	1.78
BC1I5-10-0.01-150	27.52	40.77	2.43	17.3	11.98	–	1.78
BC1I5-13-0.01-150	24.57	52.76	3.87	4.55	14.25	–	2.63
BC1I5-1-0.03-100	16.45	32.71	13.38	1.26	36.2	–	1.69
BC1I5-4-0.03-100	14.6	26.43	1.77	12.47	44.74	–	1.83
BC1I5-7-0.03-100	20.86	28.49	5.29	12.88	32.47	36.62	1.79
BC1I5-10-0.03-100	17.28	30.34	3.01	10.07	39.30	–	1.79
BC1I5-13-0.03-100	18.06	42.25	0.45	3.54	35.71	–	2.44
BC1I5-1-0.05-100	13.64	19.01	2.42	11.82	53.12	–	–
BC1I5-4-0.05-100	13.64	21.58	2.69	1053	51.56	–	–
BC1I5-7-0.05-100	14.89	20.71	2.15	11.54	50.71	29.91	–
BC1I5-10-0.05-100	13.57	23.33	1.12	9.06	52.92	–	–
BC1I5-13-0.05-100	13.96	32.36	0	3.94	49.79	–	–
BC1I5-7-0.01-100	26.53	42.36	3.15	16.58	11.38	27.14	1.80

DRS	100 °C				
pH	1	4	7	10	13
0.03	1.69	1.83	1.79	1.79	2.44
0.01	1.62	1.84	1.80	1.82	2.33
0.005	1.69	1.89	1.86	1.90	2.36
0	1.78	1.90	1.92	1.94	2.02

DRS	150 °C				
pH	1	4	7	10	13
0.03	1.57	1.77	1.69	1.62	2.23
0.01	1.78	1.87	1.78	1.78	2.63
0.005	1.80	1.86	1.88	1.86	2.97
0	1.85	1.90	1.93	1.94	2.91

(~2620 m^2g^{-1}). The pore volume and size of GO distribute to 0.016 cm^3g^{-1} and 5.32 nm. The isotherms of GO are close to Type III without a hysteresis loop at a high relative pressure between 0.6 and 1.0 [7], suggesting the existence of nonporous GO. The isotherms of BiO_xI_y and BiO_mCl_n are close to Type IV with a hysteresis loop at a high relative pressure between 0.6 and 1.0 [7]. Fig. 7 shows the nitrogen adsorption–desorption isotherm curves of $BiOCl/Bi_3O_4Cl/Bi_7O_9I_3$/BiOI/GO. The BET surface area of the samples is measured to be 27.17–36.62 m^2g^{-1}. The pore volume and size of the $BiOCl/Bi_3O_4Cl/Bi_7O_9I_3$/BiOI/GO composite sample are determined as the pore volume 0.084–0.2284 cm^3/g and 10–100 nm, respectively. The isotherms are close to Type IV with a hysteresis loop at a high relative pressure between 0.6 and 1.0. The shape of the hysteresis loop is close to H3, suggesting the existence of slit-like pores generally formed by the aggregation of plate-like particles, which is consistent with the self-assembled nanoplate-like morphology of samples. This result is consistent with the FE-SEM results, showing that self-assembled nanosheets result in the formation of hierarchical architectures.

3.2. Photocatalytic activity

Fig. 8 illustrates the changes in the ultraviolet visible (UV–vis) spectra during the photodegradation process of CV and phenol in aqueous $BiOCl/Bi_3O_4Cl/Bi_7O_9I_3$/BiOI/GO dispersions under visible light irradiation. They are wholly degraded after visible light irradiation for 72 h, approximately 99% of CV. During visible light irradiation, the characteristic absorption band of the CV dye at approximately 590.0 nm decreases rapidly with slight hypsochromic shifts (540.1 nm), but no new absorption band appears even in the ultraviolet range ($\lambda > 200$ nm), indicating the probable formation of a series of *N*-de-methylated intermediates and the cleavage of the whole conjugated chromophore structure of the CV dye. Further irradiation causes the decrease of absorption band at 540.2 nm, but no further wavelength shift is observed, inferring that the band at 540.2 nm is that of the full *N*-de-methylated product of the CV dye [6,7]. In Fig. 8(b), the characteristic absorption band of the phenol at approximately 250 nm decreases rapidly under visible light irradiation. The adsorption resulted in a decrease of about 1.3% in the phenol concentration after 0.5 h, and a decrease in the photocatalytic efficiencies of 88.6% under visible light irradiation in the phenol concentration being decomposed after 72 h, respectively.

Fig. 9 illustrates the degradation efficiency as a function of reaction time; the removal efficiency is significantly enhanced in the presence of 0.005–0.1 g BiO_pCl_q/BiO_xI_y/GO composites. To further understand the reaction kinetics of CV degradation, the apparent pseudo-first-order model [52], $ln(C_o/C) = kt$, is applied to the experiments. Through the first-order linear fit of the data shown in Fig. 9 and Table 3, the k values of BC1I5-7-0.03-100 ($BiOCl/Bi_3O_4Cl/Bi_7O_9I_3$/BiOI/GO) are obtained as the maximum degradation rates of $4.22 \times 10^{-1}\ h^{-1}$ by using the first-order linear fit of the data, which are much higher than those of the other composites. The BC1I5-7-0.03-100 composite has largest S_{BET} (Table 2). However, the result in Table 2 shows that the BC1I5-7-0.03-100 sample—which does show the highest S_{BET}—does represent the highest photocatalytic activity ($k = 4.22 \times 10^{-1}\ h^{-1}$) among the samples, suggesting that the changes in the photocatalytic activity are resulted from both S_{BET} and BiO_pCl_q/BiO_xI_y/GO composites. Table 3 shows a comparison among the rate constants of different photocatalysts. The order of rate constants shows $BiOCl/Bi_3O_4Cl/BiOI/Bi_7O_9I_3$/GO > $BiOCl/Bi_{12}O_{17}Cl_2$/BiOI/GO > $BiOCl/Bi_{12}O_{17}Cl_2$/BiOI/GO > $BiOCl/Bi_3O_4Cl/BiOI/Bi_7O_9I_3$/GO > $Bi_{12}O_{17}Cl_2/Bi_5O_7I$/GO >

Table 3
Pseudo-first-order rate constants for the degradation of CV with photocatalysts under visible light irradiation.

Sample Code	Rate constant	GO (g)					
		0	0.005	0.01	0.03	0.05	0.1
BC1I5-1-GO-100 (BiOCl/BiOI/GO)	k	0.026	0.026	0.017	0.044	0.078	0.066
	R^2	0.99	0.97	0.99	0.98	0.99	0.79
BC1I5-4-GO-100 (BiOCl/BiOI/GO)	k	0.109	0.101	0.156	0.167	0.173	0.147
	R^2	0.90	0.96	0.97	0.99	0.96	0.93
BC1I5-7-GO-100 ($BiOCl/Bi_3O_4Cl/BiOI/Bi_7O_9I_3$/GO)	k	0.182	0.188	0.294	**0.422**	0.329	–
	R^2	0.97	0.99	0.90	0.99	0.97	–
BC1I5-10-GO-100 ($BiOCl/Bi_{12}O_{17}Cl_2$/BiOI/GO)	k	0.268	0.334	0.200	0.278	–	–
	R^2	0.99	0.99	0.99	0.97	–	–
BC1I5-13-GO-100 ($Bi_{12}O_{17}Cl_2/Bi_5O_7I$/GO)	k	0.096	0.088	0.944	0.002	–	–
	R^2	0.96	0.98	0.96	0.38	–	–
BC1I5-1-GO-150 (BiOCl/BiOI/GO)	k	0.040	0.062	0.084	0.068	–	–
	R^2	0.91	0.95	0.97	0.95	–	–
BC1I5-4-GO-150 (BiOCl/BiOI/GO)	k	0.091	0.073	0.089	0.127	0.251	0.121
	R^2	0.99	0.99	0.88	0.99	0.97	0.98
BC1I5-7-GO-150 ($BiOCl/Bi_3O_4Cl/BiOI/Bi_7O_9I_3$/GO)	k	0.178	0.151	0.212	0.281	0.239	–
	R^2	0.99	0.99	0.99	0.98	0.85	–
BC1I5-10-GO-150 ($BiOCl/Bi_{12}O_{17}Cl_2$/BiOI/GO)	k	0.234	0.277	0.325	0.306	–	–
	R^2	0.97	0.97	0.98	0.97	–	–
BC1I5-13-GO-150 ($Bi_{12}O_{17}Cl_2/Bi_5O_7I$/GO)	k	0.002	0.003	0.002	0.147	0.013	–
	R^2	0.803	0.958	0.868	0.994	0.971	–

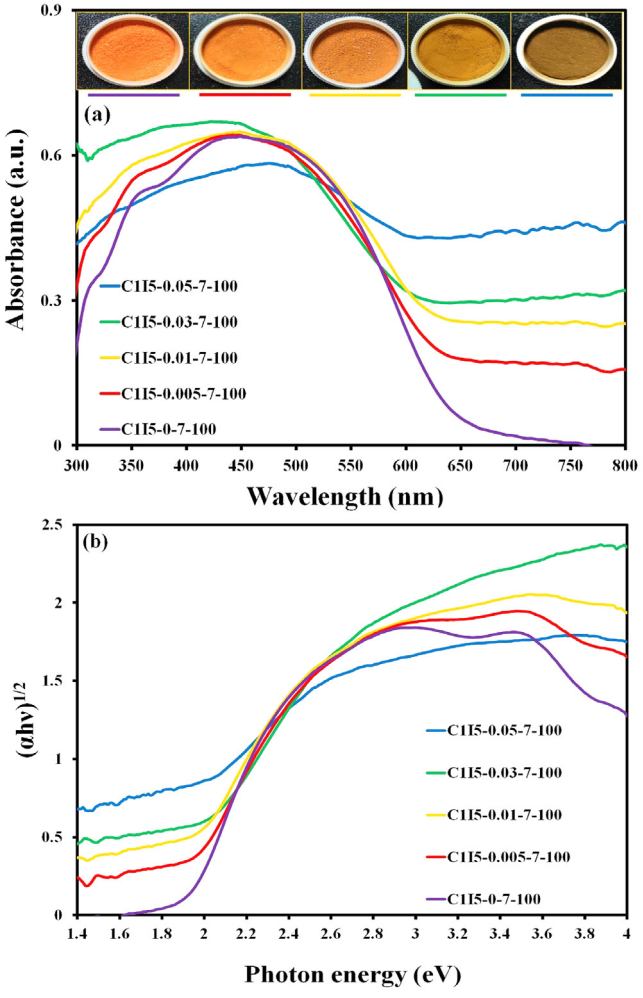

Fig. 6. DRS patterns of as-prepared $BiOCl/Bi_3O_4Cl/Bi_7O_9I_3$/BiOI/GO samples under pH 7.

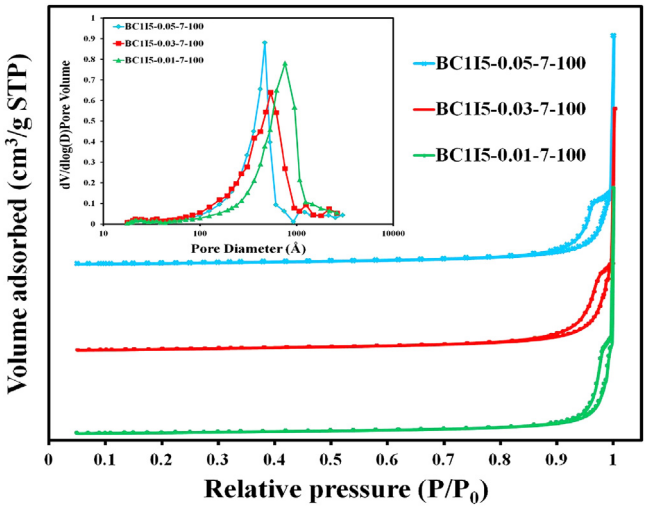

Fig. 7. N_2 adsorption-desorption isotherm and pore size distribution surface area of $BiOCl/Bi_3O_4Cl/Bi_7O_9I_3$/BiOI/GO with different GO weight (g) at pH 7.

$Bi_{12}O_{17}Cl_2/Bi_5O_7I$/GO > $Bi_4O_5I_2$ > $Bi_7O_9I_3$ > BiOI > Bi_5O_7I > BiOCl > GO. The photocatalytic activity of $BiOCl/Bi_3O_4Cl/BiOI/Bi_7O_9I_3$/GO composites reaches a maximum rate constant of 0.422 h^{-1}, which is 2.3 times higher than that of $BiOCl/Bi_3O_4Cl/BiOI/Bi_7O_9I_3$, 9 and 2 times higher than that of BiOI and $Bi_4O_5I_2$, and 18 and 12 times higher than that of BiOCl and Bi_3O_4Cl.

However, the photocatalytic activity over the BiO_pCl_q/BiO_xI_y/GO nanocomposites decreases when the GO content exceeds approximately 0.03 g. This decrease may be attributed to the joint effect between the excellent charge transfer capability of GO and its detrimental effect on visible light absorption. The durability of BC1I5-7-0.03-100 ($BiOCl/Bi_3O_4Cl/Bi_7O_9I_3$/BiOI/GO) composite is evaluated by recycling the used catalyst. After each cycle, the catalyst is collected by centrifugation. No apparent loss is observed in the photocatalytic activity when CV is removed in the 3rd cycle; even during the fifth run, the decline in photocatalytic activity appears 5% (Fig. 10(a)). The used BC1I5-7-0.03-100 composite is

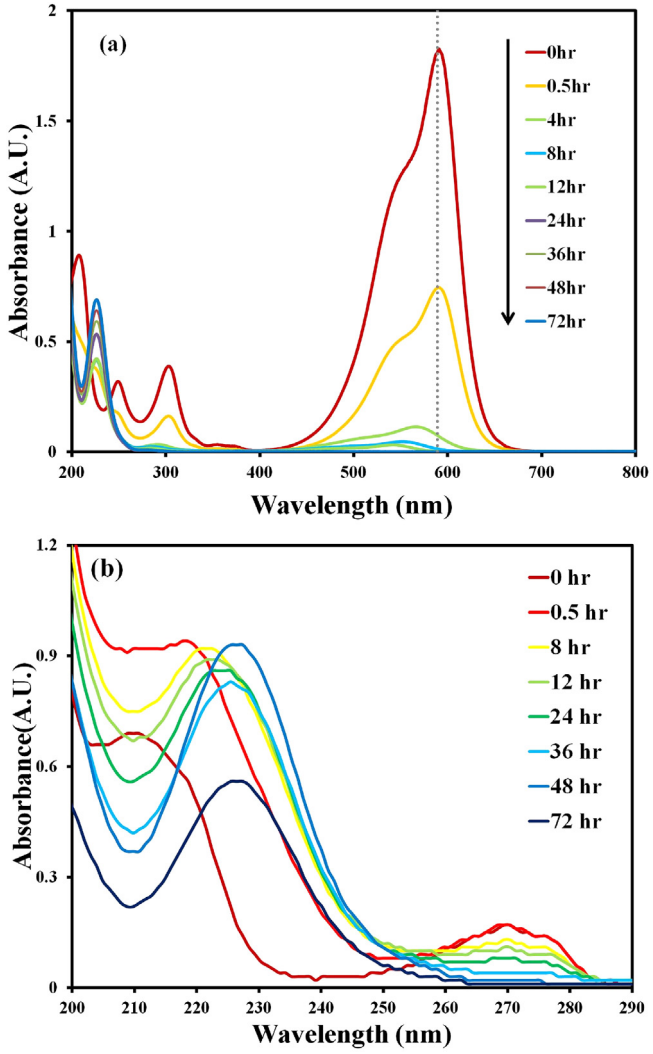

Fig. 8. Temporal UV–vis adsorption spectral of (a) CV and (b) phenol changes during the photocatalytic degradation of CV over aqueous $BiOCl/Bi_3O_4Cl/Bi_7O_9I_3/BiOI/GO$ under visible light irradiation.

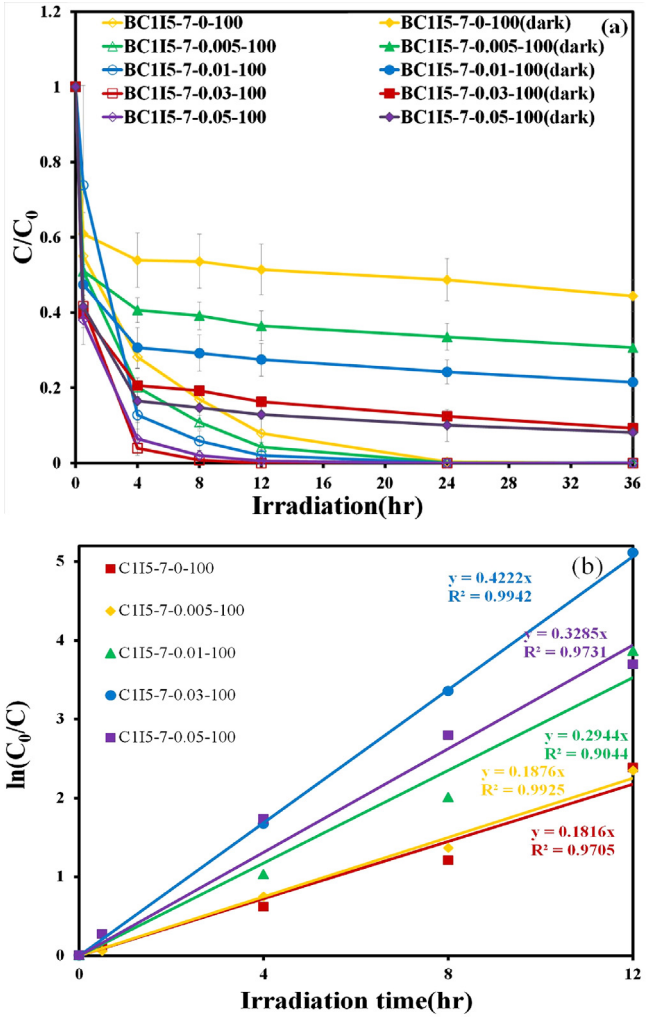

Fig. 9. Photodegradation of CV as a function of irradiation time over different $BiOCl/Bi_3O_4Cl/BiOI/Bi_7O_9I_3/GO$ photocatalysts. (GO = 0.005–0.05 g, Molar ratio KCl: KI = 1: 5, $Bi(NO_3)_3{\cdot}5H_2O$ = 2.42 g, KI = 15 mmol, KCl = 3 mmol, hydrothermal conditions: temp = 100 °C, pH = 7, time = 12 h).

also examined by XRD and no detectable difference is observed between the as-prepared and the used samples (Fig. 10(b)); hence, the BC1I5-7-0.03-100 ($BiOCl/Bi_3O_4Cl/Bi_7O_9I_3/BiOI/GO$) composite has excellent photostability.

Photocatalysts are excited to generate electron–hole pairs directly after the illumination in the photocatalytic process. Photocatalytic efficiency depends mainly on the recombination rate or the lifetime of the photogenerated electron–hole pairs. The faster the recombination occurs, the shorter the chemical reaction time is. Therefore, PL spectra are utilized for investigating the recombination rate of the photogenerated electron–hole pairs [53]. To investigate the separation capacity of the photogenerated carriers in the heterostructures, the PL spectra of $BiOCl/Bi_3O_4Cl/Bi_7O_9I_3/BiOI/GO$ with 0–0.05 g GO weight are measured; the results are shown in Fig. 11. A weak emission peak at approximately 550 nm appears on the as-prepared samples, which could have been derived from the direct electron–hole recombination of band transitions. However, the characteristic emission peak within the low intensity 550 nm for $BiOCl/Bi_3O_4Cl/Bi_7O_9I_3/BiOI/GO$ with 0–0.05 g GO weight indicates that the recombination of photogenerated charge carriers is greatly inhibited. The efficient separation of charge could increase the lifetime of charge carriers and enhance the efficiency of interfacial charge transfer to the adsorbed substrates, thus improving the photocatalytic activity [50]. The PL results confirm the importance of the composites in hindering the recombination of electrons and holes and explain the reason for the increasing photocatalytic performance of $BiO_pCl_q/BiO_xI_y/GO$ composites.

Presumably, the enhanced photocatalytic activities of $BiO_pCl_q/BiO_xI_y/GO$ composites could be ascribed to a synergistic effect including a high BET surface area, the formation of the composites (or heterojunction), a layered structure, and the low energy band structure. In the absence of photocatalysts, CV could not be degraded under visible light irradiation; the superior photocatalytic ability of $BiO_pCl_q/BiO_xI_y/GO$ may be ascribed to its efficient utilization of visible light and high separation efficiency of the electron–hole pairs within its composites.

3.3. Active Species

In general, three proposed possible reaction mechanisms are involved in the photodegradation of organisms by a semiconductor, including (i) photocatalysis, (ii) photolysis, and (iii) dye photosensitization [54]. In the photolysis process, a photoinduced electron on the induced organism directly reacts with O_2 to produce a single oxygen atom that acts as an oxidant for the pure organism photolysis [55]. In the present experiments, CV degradation caused by

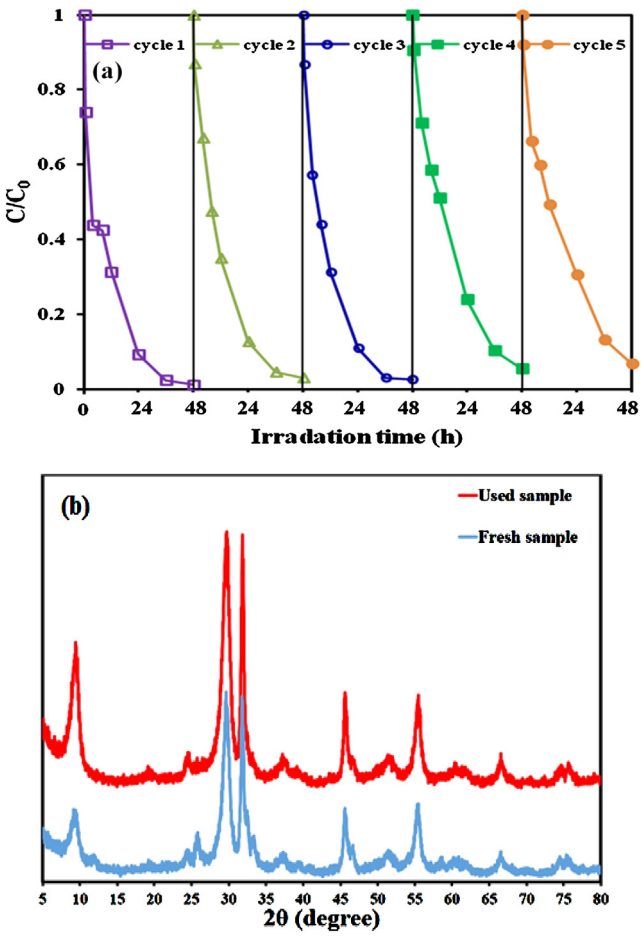

Fig. 10. (a) Cycling runs in the photocatalytic degradation of CV in the presence of BC1I5-7-0.03-100 ($BiOCl/Bi_3O_4Cl/Bi_7O_9I_3/BiOI/GO$); (b) XRD of powder sample before and after the degradation reaction.

photolysis under visible light in a blank experiment is not observable; CV is a structure-stable dye, and the decomposition by the photolysis mechanism is negligible.

Various primary active species, such as hydroxyl radical, hole, superoxide radical, hydrogen radical ($H^{\bullet}$), and singlet oxygen, could be generated during photo-catalytic decomposition processes in UV–vis/semiconductor systems [21]. Dimitrijevic et al. [56] proposed that water, which dissociated both on the surface of TiO_2 and in subsequent molecular layers, had a three-fold role as (i) a stabilizer of charges, preventing electron–hole recombination; (ii) as an electron acceptor, forming H atoms in a reaction of photogenerated electrons with protons on the surface, $-OH_2^+$; and (iii) an electron donor, resulting in the reaction of water with photogenerated holes to give $^{\bullet}OH$ radicals.

When GO is combined with other materials, electrons would flow from one material to another (from a higher to a lower Fermi level) to align the Fermi energy levels at the interface of two materials [57]. Bai et al. [58] reported that active species trapping measurements, superoxide radicals ($O_2^{-\bullet}$) and hydroxy radicals ($^{\bullet}OH$) played a crucial role during the catalytic process in the methylene blue degradation process using $ZnWO_4$/graphene hybrids. Wang et al. [59] revealed that $O_2^{-\bullet}$ and $^{\bullet}OH$ were the main reactive species for the degradation of rhodamine B with $BiVO_4$/rGO. Shenawi-Khalil et al. [60] reported that $^{\bullet}OH$ radicals were generated through the multistep reduction of $O_2^{-\bullet}$. The generation of $O_2^{-\bullet}$ could not only inhibit the recombination of photoinduced charge carriers but also benefit the de-chlorination

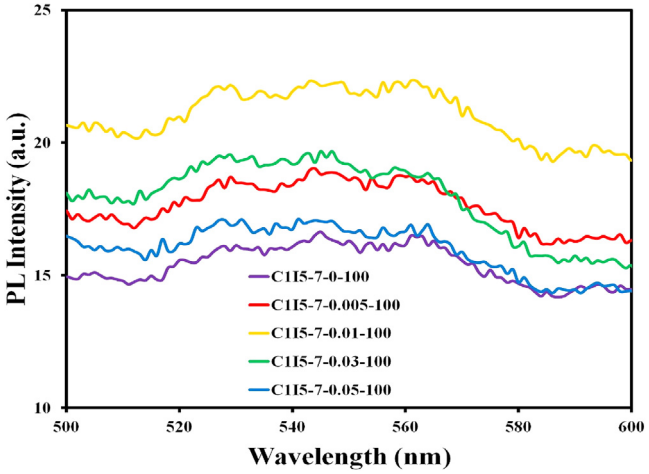

Fig. 11. PL spectrum of $BiOCl/Bi_3O_4Cl/Bi_7O_9I_3/BiOI/GO$ with different GO weights at pH 7.

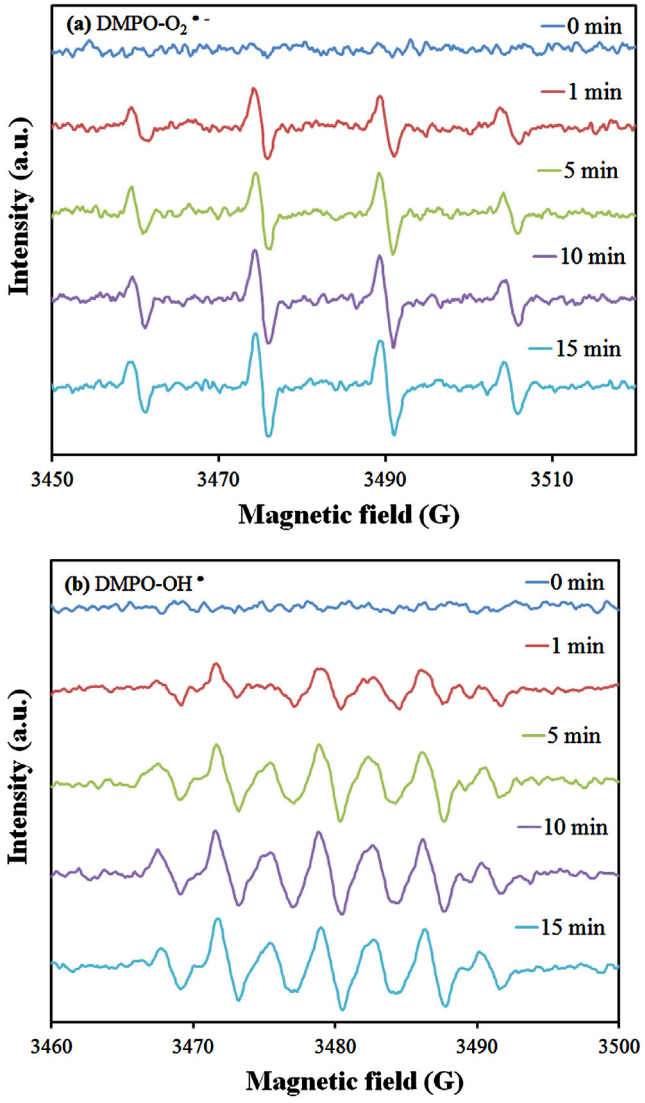

Fig. 12. (a), (b) DMPO spin trapping EPR spectra for DMPO–O_2^- and DMPO–OH under visible light irradiation with $Bi_3O_4Cl/BiOCl/BiOI/Bi_7O_9I_3/GO$ photocatalyst. (c) The dye concentration during photodegradation as a function of irradiation time observed in $Bi_3O_4Cl/BiOCl/BiOI/Bi_7O_9I_3/GO$ photocatalyst under the addition of different scavengers of SA, IPA, AQ, and BQ.

of chlorinated phenol derivative. The hydroxyl radical HO• might only be formatted through an $e^- \rightarrow O_2^{-\bullet} \rightarrow H_2O_2 \rightarrow {}^\bullet OH$ route. However, •OH radical was formatted through the multistep reduction of $O_2^{-\bullet}$ in the system [61]. Jiang et al. [62] reported that the g-C_3N_4/BiOBr-mediated photodegradation of methylene blue molecules was attributed mainly to the oxidation action of the generated $O_2^{-\bullet}$ radicals and partly to the action of h^+ through the direct hole oxidation process. According to a previous study [58], a photocatalytic process was governed mainly by $O_2^{-\bullet}$ rather than by •OH, e^-, or h^+. In a previous study [5], the CV photodegradation by BiO_mX_n/BiO_pY_q (X, Y = Cl, Br, I) under visible light was dominated by oxidation with $O_2^{-\bullet}$ being the main active species and •OH and h^+ being the minor active species. On the basis of the aforementioned references, the probability of forming •OH should be much lower than that for $O_2^{-\bullet}$; however, •OH is an extremely strong and nonselective oxidant, which leads to a partial or complete mineralization of several organic chemicals.

Fig. 12(a) and (b) shows not only the four characteristic peaks (strong) of DMPO-•OH adducts (1:2:2:1 quartet pattern) but also the six characteristic peaks of DMPO-$O_2^{-\bullet}$ adducts under visible light irradiating BiOCl/Bi_3O_4Cl/$Bi_7O_9I_3$/BiOI/GO composite dispersion. Fig. 12(a) and (b) indicates that no electron paramagnetic resonance (EPR) signal is observed when the reaction is performed in the dark, whereas the signals with intensity corresponding to the characteristic peak of DMPO-•OH and DMPO-$O_2^{-\bullet}$ adducts [18] are observed during the reaction process under visible light irradiation, suggesting that $O_2^{\bullet-}$ and hydroxyl radical (•OH) as active species are formed in the presence of BiOCl/Bi_3O_4Cl/$Bi_7O_9I_3$/BiOI/GO composites and oxygen under visible light irradiation.

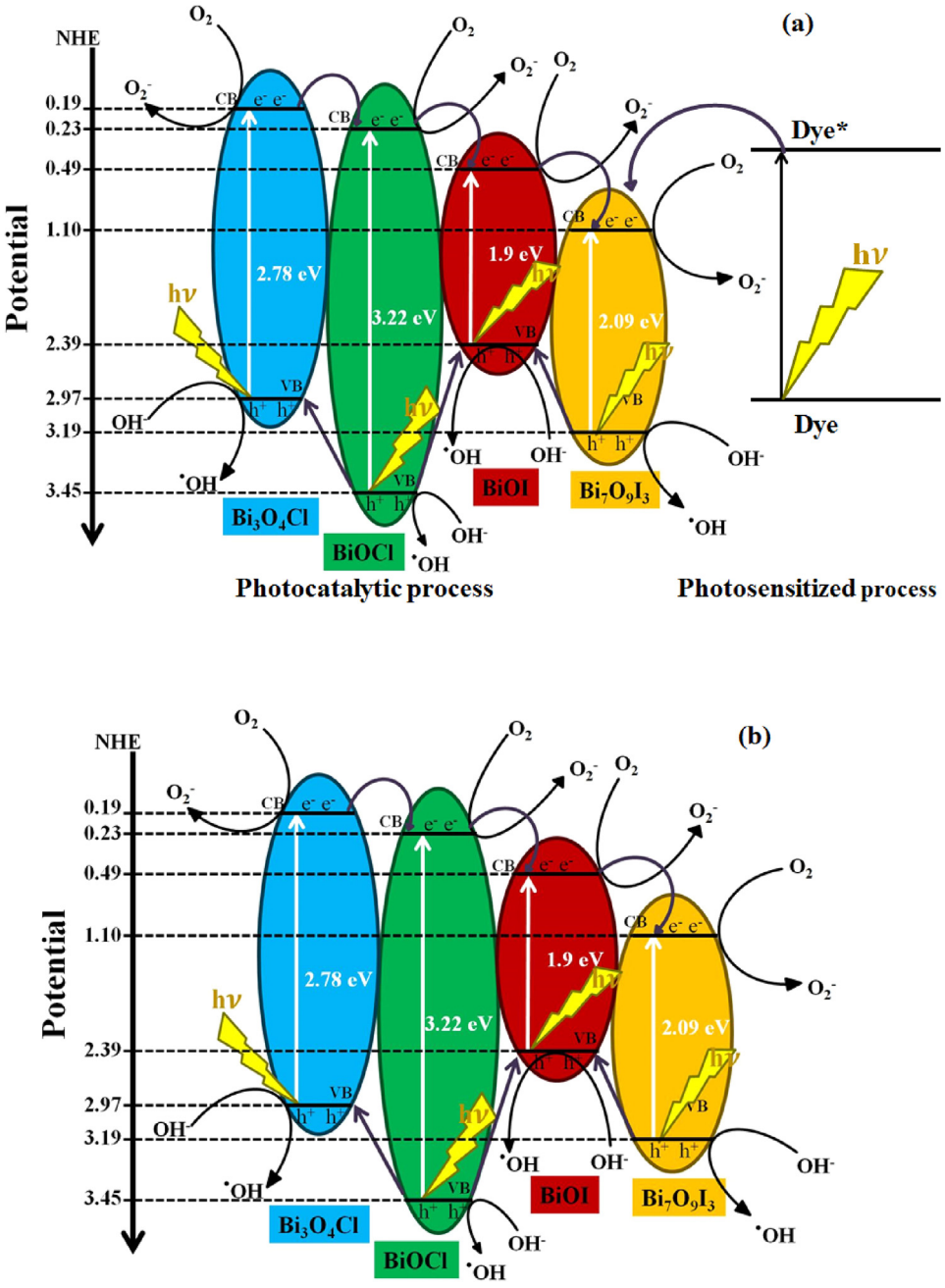

Fig. 13. Schematic illustration of the band gap structures of Bi_3O_4Cl/BiOCl/BiOI/$Bi_7O_9I_3$/GO and the possible charge separation processes. (a) CV (b) Phenol.

To re-evaluate the effect of the active species during the photocatalytic reaction, a series of quenchers are introduced to scavenge the relevant active species. As shown in Fig. 12(c), the photocatalytic degradation of CV is not affected by the addition of AO, whereas the degradation efficiency of BQ, IPA, and SA quenching evidently decrease when compared with that of no quenching. $O_2^{\bullet-}$ is a major active species and $^{\bullet}OH$ and $^1O_2$ are minor active species in the process of photocatalytic degradation of CV. Therefore, the quenching effects of different scavengers and EPR indicate that reactive $O_2^{\bullet-}$ plays a major role and $^{\bullet}OH$ and $^1O_2$ play a minor role in CV photocatalytic degradation.

On the basis of the aforementioned experimental results, a detailed pathway of decomposition is illustrated in Fig. 13. Once the electron reaches the conduction band of BiO_xX_y (X = Cl, I), it induces the formation of active oxygen species, which causes the decomposition of CV dye and phenol. Both photo-sensitized and photo-catalytic processes are proceeded concurrently (Fig. 13(a)). The photo-catalytic processes are proceeded concurrently (Fig. 13(b)). However, in photo-sensitized and photocatalytic reaction conditions, $O_2^{\bullet-}$ radicals are formatted by the reaction of photogenerated and photosensitized electron with oxygen gas on the photocatalyst surface; hydroxyl radicals are also produced by the reaction of $O_2^{\bullet-}$ radicals with H^+ ion and hole h^+ with OH^- ion (or H_2O). The hydroxyl radicals are produced subsequently [63]. This cycle continuously occurs when the system is exposed to visible light irradiation [8]; To understand this unexpected result, the mechanism of $^1O_2$ formation is more closely examined during photoexcitation of BiO_pCl_q/BiO_xI_y/GO photocatalyst. $^1O_2$ also can be produced via the electron transfer between superoxide $O_2^{\bullet-}$ and cation species with appropriate oxidizing power [64]. Photogenerated h^+ in semiconductor nanoparticles could be such cation species to oxidize $O_2^{\bullet-}$. This mechanism for the production of $^1O_2$ during photoexcitation of ZnO has been reported [65]; after several cycles of photooxidation, the decomposition of CV and phenol by the generated oxidant species can be expressed by Eqs. (16)–(18).

$$CV(orphenol) + O_2^{-\bullet} \rightarrow decomposedcompounds \quad (16)$$

$$CV(orphenol) + OH^{\bullet} \rightarrow decomposedcompounds \quad (17)$$

$$CV(orphenol) + {}^1O_2 \rightarrow decomposedcompounds \quad (18)$$

Hydroxylated compounds are identified for the photocatalytic degradation of CV under visible light-induced semiconductor systems [5]. Under UV light irradiation, *N*-dealkylation processes are preceded by the formation of a nitrogen-centered radical, and the destruction of the dye chromophore structure is preceded by the generation of a carbon-centered radical in the photocatalytic degradation of the CV dye [7,8,63]. All the intermediates identified in these two researched topics have the same results under UV or visible light irradiation. Undoubtedly, the major oxidant is $^{\bullet}OH$ radicals, not $O_2^{-\bullet}$ radicals. The reaction pathways of BiO_xI_y/GO-mediated photocatalytic processes proposed in this study should offer some guidance for applications in the decomposition of dyes.

4. Conclusions

This is the first report where BiO_pCl_q/BiO_xI_y/GO-assisted photocatalytic degradation of the CV dye and phenol under visible light irradiation is synthesized through a simple hydrothermal method. The assembled $Bi_3O_4Cl/BiOCl/BiOI/Bi_7O_9I_3$/GO exhibits excellent photocatalytic activity in the degradation of CV under visible light irradiation. The order of rate constants presents $BiOCl/Bi_3O_4Cl/BiOI/Bi_7O_9I_3$/GO > $BiOCl/Bi_{12}O_{17}Cl_2/BiOI$/GO > $BiOCl/Bi_{12}O_{17}Cl_2/BiOI$/GO > $BiOCl/Bi_3O_4Cl/BiOI/Bi_7O_9I_3$/GO > $Bi_{12}O_{17}Cl_2/Bi_5O_7I$/GO > $Bi_4O_5I_2$ > $Bi_7O_9I_3$ > BiOI > Bi_5O_7I > BiOCl > GO. Thus, the $Bi_3O_4Cl/BiOCl/BiOI/Bi_7O_9I_3$/GO composites play a major role in enhancing photocatalytic activity. The quenching effects of different scavengers and EPR demonstrat that reactive $O_2^{\bullet-}$ plays a major role and $^1O_2$ and $^{\bullet}OH$ play a minor role in CV degradation. Chiefly, composite systems exhibit adequate catalytic activity and stability, acting as authentic heterogeneous visible-light-driven photocatalysts in degrading organic pollutants efficiently.

Acknowledgments

This research was supported by the Ministry of Science and Technology of the Republic of China (NSC-104-2113-M-142-001).

References

[1] Kubacka, G. Fernández-García, G. Colón, Chem. Rev. 112 (2012) 1555–1614.
[2] F. Chen, P. Fang, Y. Gao, Z. Liu, Y. Liu, Y. Dai, Chem. Eng. J. 204–206 (2012) 107–113.
[3] S. Ameen, M.S. Akhtar, M. Nazim, H.S. Shin, Mater. Lett. 96 (2013) 228–232.
[4] W.L.W. Lee, W.H. Chung, W.S. Huang, W.C. Lin, W.Y. Lin, Y.R. Jiang, C.C. Chen, J. Taiwan Inst. Chem. Eng. 44 (2013) 660–669.
[5] W.W. Lee, C.S. Lu, C.W. Chuang, Y.J. Chen, J.Y. Fu, C.W. Siao, C.C. Chen, RSC Adv. 5 (2015) 23450–23463.
[6] W.L.W. Lee, J.S. Lin, J.L. Chang, J.Y. Chen, M.C. Cheng, C.C. Chen, J. Mol. Catal. A: Chem. 361–362 (2012) 80–90.
[7] Y.R. Jiang, H.P. Lin, W.H. Chung, Y.M. Dai, W.Y. Lin, C.C. Chen, J. Hazard. Mater. 283 (2015) 787–805.
[8] Y.R. Jiang, S.Y. Chou, J. Lin Chang, S.T. Huang, H.P. Lin, C.C. Chen, RSC Adv. 5 (2015) 30851–30860.
[9] K. Yu, S. Yang, C. Liu, H. Chen, H. Li, C. Sun, S.A. Boyd, Environ. Sci. Technol. 46 (2012) 7318–7326.
[10] H.P. Lin, C.C. Chen, W.W. Lee, Y.Y. Lai, J.Y. Chen, Y.Q. Chen, J.Y. Fu, RSC Adv. 6 (2016) 2323–2336.
[11] C.T. Yang, W.W. Lee, H.P. Lin, Y.M. Dai, H.T. Chi, C.C. Chen, RSC Adv. 6 (2016) 40664–40675.
[12] S.Y. Chou, W.H. Chung, L.W. Chen, Y.M. Dai, W.Y. Lin, J.H. Lin, C.C. Chen, RSC Adv. 6 (2016) 82743–82758.
[13] W. Wang, M.O. Tadé, Z. Shao, Chem. Soc. Rev. 44 (2015) 5371–5408.
[14] S. Gupta, V. Subramanian, ACS Appl. Mater. Interfaces 6 (2014) 18597–18608.
[15] H. Cheng, B. Huang, Y. Dai, Nanoscale 6 (2014) 2009–2026.
[16] Jie Li, Ying Yu, Lizhi Zhang, Nanoscale 6 (2014) 8473–8488.
[17] Y. Huo, J. Zhang, M. Miao, Y. Jin, Appl. Catal. B: Environ. 111–112 (2012) 334–341.
[18] X. Xiao, C. Xing, G. He, X. Zuo, J. Nan, L. Wang, Appl. Catal. B: Environ. 148–149 (2014) 154–163.
[19] R. Zhou, J. Wu, J. Zhang, H. Tian, P. Liang, T. Zeng, P. Lu, J. Ren, T. Huang, X. Zhou, P. Sheng, Appl. Catal. B: Environ. 204 (2017) 465–474.
[20] X. Jia, J. Cao, H. Lina, M. Zhang, X. Guo, S. Chen, Appl. Catal. B: Environ. 204 (2017) 505–514.
[21] Y. Peng, K.K. Wang, T. Liu, J. Xu, B.G. Xu, Appl. Catal. B: Environ. 203 (2017) 946–954.
[22] W.L. Huang, Q.S. Zhu, J. Comput. Chem. 30 (2009) 183–190.
[23] X. Xiao, C. Liu, R. Hu, X. Zuo, J. Nan, L. Li, L. Wang, J. Mater. Chem. 22 (2012) 22840–22843.
[24] E. Keller, V. Kramer, Z. Naturforsch 60b (2005) 1255–1263.
[25] Q. Xiang, J. Yu, M. Jaroniec, Chem. Soc. Rev. 41 (2012) 782–796.
[26] H. Liu, W.R. Cao, Y. Su, Z. Chen, Y. Wang, J. Colloid Interface Sci. 398 (2013) 161–167.
[27] X.X. Wei, C.M. Chen, S.Q. Guo, F. Guo, X.M. Li, X.X. Wang, H.T. Cui, L.F. Zhao, W. Li, J. Mater. Chem. A. 2 (2014) 4667–4675.
[28] I.V. Lightcap, T.H. Kosel, P.V. Kamat, Nano Lett. 10 (2010) 577–583.
[29] S. Song, B. Cheng, N. Wu, A. Meng, S. Cao, J. Yu, Appl. Catal. B: Environ. 181 (2016) 71–78.
[30] K. Chang, Z. Mei, T. Wang, Q. Kang, S. Ouyang, J. Ye, ACS Nano 8 (2014) 7078–7087.
[31] A. Bhirud, S. Sathaye, R. Waichal, C.J. Park, B. Kale, J. Mater. Chem. A 3 (2015) 17050–17063.
[32] W.K. Jo, S. Kumar, M.A. Isaacs, A.F. Lee, S. Karthikeyan, Appl. Catal. B: Environ. 201 (2017) 159–168.
[33] N. Yang, Y. Liu, H. Wen, Z. Tang, H. Zhao, Y. Li, D. Wang, ACS Nano 7 (2013) 1504–1512.
[34] Y. Wang, W. Wang, H. Mao, Y. Lu, J. Lu, J. Huang, Z. Ye, B. Lu, ACS Appl. Mater. Interfaces 6 (2014) 12698–12706.
[35] Y.C. Yang, L. Xu, W.Q. Huang, C.Y. Luo, G.F. Huang, P. Peng, J. Phys. Chem. C 119 (2015) 19095–19104.
[36] T. Soltani, B.K. Lee, Chem. Eng. J. 306 (2016) 204–213.
[37] H. Liu, Y. Su, Z. Chen, Z. Jin, Y. Wang, J. Mol. Catal. A: Chem. 391 (2014) 175–182.
[38] H. Huang, K. Liu, Y. Zhang, K. Chen, Y. Zhang, N. Tian, RSC Adv. 4 (2014) 49386–49394.

[39] W.S. Hummers, R.E. Offeman, J. Am. Chem. Soc. 80 (1958) 1339.
[40] M.C. Yin, Z.S. Li, J.H. Kou, Z.G. Zou, Environ. Sci. Technol. 43 (2009) 8361–8366.
[41] L.S. Zhang, K.H. Wong, H.Y. Yip, C. Hu, J.C. Yu, C.Y. Chan, P.K. Wong, Environ. Sci. Technol. 44 (2010) 1392–1398.
[42] S.G. Meng, D.Z. Li, M. Sun, W.J. Li, J.X. Wang, J. Chen, X.Z. Fu, G.C. Xiao, Catal. Commun. 12 (2011) 972–975.
[43] G. Li, K.H. Wong, X. Zhang, C. Hu, J.C. Yu, R.C.Y. Chan, P.K. Wong, Chemosphere 76 (2009) 1185–1191.
[44] X. Xiao, W.D. Zhang, RSC Adv. 1 (2011) 1099–1105.
[45] H. Liu, Y. Su, Z. Chen, Z. Jin, Y. Wang, J. Mol. Catal. A: Chem. 391 (2014) 175–182.
[46] C. Nethravathi, M. Rajamathi, Carbon 46 (2008) 1994–1998.
[47] P. Dong, Y. Wang, B. Cao, S. Xin, H.L. Guo, J. Zhang, F. Li, Appl. Catal. B: Environ. 132–133 (2013) 45–53.
[48] A.V. Murugan, T. Muraliganth, A. Manthiram, Rapid. Chem. Mater. 21 (2009) 5004–5006.
[49] Y.R. Jiang, H.P. Lin, W.H. Chung, Y.M. Dai, W.Y. Lin, C.C. Chen, J. Hazard. Mater. 283 (2015) 787–805.
[50] F. Dong, Y. Sun, M. Fu, Z. Wu, S.C. Lee, J. Hazard. Mater. 219–220 (2012) 26–34.
[51] D. Chen, H. Feng, J. Li, Chem. Rev. 112 (2012) 6027–6053.
[52] A. Chatzitakis, C. Berberidou, I. Paspaltsis, G. Kyriakou, T. Sklaviadis, I. Poulios, Water Res. 42 (2008) 386–394.
[53] K. Ishibashi, A. Fujishima, T. Watanabe, K. Hashimoto, Electrochem. Commun. 2 (2000) 207–210.
[54] C. Nasr, K. Vinodgopal, L. Fisher, S. Hotchandani, A.K. Chattopadhyay, P.V. Kamat, J. Phys. Chem. 100 (1996) 8436–8442.
[55] X. Xiao, R. Hao, M. Liang, X. Zuo, J. Nan, L. Li, W. Zhang, J. Hazard. Mater. 233–234 (2012) 122–130.
[56] N.M. Dimitrijevic, B.K. Vijayan, O.G. Poluektov, T. Rajh, K.A. Gray, H. He, P. Zapol, J. Am. Chem. Soc. 133 (2011) 3964–3971.
[57] H.Y. Mao, S. Laurent, W. Chen, O. Akhavan, M. Imani, A.A. Ashkarran, M. Mahmoudi, Chem. Rev. 113 (2013) 3407–3424.
[58] X. Bai, L. Wang, Y. Zhu, ACS Catal. 2 (2012) 2769–2778.
[59] Y. Wang, W. Wang, H. Mao, Y. Lu, J. Lu, J. Huang, Z. Ye, B. Lu, ACS Appl. Mater. Interfaces 6 (2014) 12698–12706.
[60] S. Shenawi-Khalil, V. Uvarov, S. Fronton, I. Popov, Y. Sasson, J. Phys. Chem. C 116 (2012) 11004–11012.
[61] S.T. Huang, Y.R. Jiang, S.Y. Chou, Y.M. Dai, C.C. Chen, J. Mol. Catal. A: Chem. 391 (2014) 105–120.
[62] D.L. Jiang, L. l. Chen, J.J. Zhu, M. Chen, W.D. Shi, J.M. Xie, Dalton Trans. 42 (2013) 15726–15734.
[63] H.J. Fan, C.S. Lu, W.L.W. Lee, M.R. Chiou, C.C. Chen, J. Hazard. Mater. 185 (2011) 227–235.
[64] W. He, H. Jia, W.G. Wamer, Z. Zheng, P. Li, J.H. Callahan, J.J. Yin, J. Catal. 320 (2014) 97–105.
[65] W. He, H.K. Kim, W.G. Wamer, D. Melka, J.H. Callahan, J.J. Yin, J. Am. Chem. Soc. 136 (2014) 750–757.